International Journal of Computational and Experimental Science and ENgineering
(IJCESEN)
Vol. 12-No.1 (2025) pp. 1321-1335
http://www.ijcesen.com
ISSN: 2149-9144

Copyright © IJCESEN

Research Article

SCAPS-1D Numerical Optimization of ZnO:Al/PCBM/$CsSnI_3$/MoO_3 Perovskite Solar Cells

Zineb Ibtissem Gouchida[1,2*], Yazid Benbouzid[3,4], Mostefa Maache[5,6], Zehor Allam[7]

[1]University of Djelfa, FECS, Ziane Achour University, 17000 Djelfa, Algeria
[2]Physico-Chemistry of Materials and Environment Laboratory, Ziane Achour University of Djelfa, BP 3117 Djelfa, Algeria
* **Corresponding Author Email:** ibtissam.gouchida@gmail.com - **ORCID:** 0009-0004-0332-5940

[3]University of Djelfa, FECS, Ziane Achour University, 17000 Djelfa, Algeria
[4]Physico-Chemistry of Materials and Environment Laboratory, Ziane Achour University of Djelfa, BP 3117 Djelfa, Algeria
Email: y.benbouzid@univ-djelfa.dz - **ORCID:** 0000-0002-7662-0789

[5]University of Djelfa, FECS, Ziane Achour University, 17000 Djelfa, Algeria
[6]Laboratory of Physics of Thin Films and Applications, Mohamed Khider University, Biskra, Algeria.
Email: zh1344@yahoo.fr - **ORCID:** 0009-0006-2249-7398

[7]Laboratory of Telecommunication and Smart Systems (LTSS), Faculty of Science and Technology University of Djelfa, PO Box 3117, Djelfa 17000, Algeria;
Email: m.maache@univ-djelfa.dz - **ORCID:** 0000-0002-1434-909X

Article Info:

DOI: 10.22399/ijcesen.5020
Received : 27 Decemer 2025
Revised : 25 February 2026
Accepted : 07 March 2026

Keywords

$CsSnI_3$
solar cells
SCAPS-1D
perovskites
optimization

Abstract:

A numerical optimization of lead-free ZnO:Al/PCBM/$CsSnI_3$/MoO_3 perovskite solar cells is performed using the SCAPS-1D simulator. The effects of absorber and transport layer thickness, doping concentration, defect density, series and shunt resistances, and operating temperature on device performance are systematically investigated. The results show that the $CsSnI_3$ absorber thickness and defect density dominate recombination losses and efficiency, while the PCBM layer exhibits strong defect tolerance. Optimized absorber thickness (1.2 µm) and acceptor doping (10^{19} cm^{-3}) significantly enhance charge collection and fill factor. Series resistance strongly degrades performance, whereas high shunt resistance is essential for achieving high open-circuit voltage. Under optimized conditions, a maximum power conversion efficiency of 25.39% is achieved, representing a theoretical upper limit for $CsSnI_3$-based single-junction solar cells. The study provides clear guidelines for defect passivation and interface engineering in lead-free perovskite photovoltaics.

1. Introduction

As global efforts to decarbonize energy systems intensify, the development of photovoltaic (PV) technologies that are not only scalable and efficient but also environmentally sustainable has become a critical priority. Among the most promising candidates, hybrid lead-halide perovskites have emerged as frontrunners, achieving power conversion efficiencies (PCE) exceeding 25% within a single decade an unprecedented leap in solar energy research and development [1,2]. Despite this remarkable progress, their widespread commercialization is impeded by major drawbacks, primarily the inherent toxicity of lead and long-term material instability, both of which raise serious environmental and durability concerns [3].

In response to these limitations, research has increasingly focused on lead-free alternatives, particularly cesium tin iodide ($CsSnI_3$), which combines an environmentally benign composition with attractive optoelectronic properties [4]. $CsSnI_3$ features a direct bandgap of approximately 1.3 eV near the Shockley-Queisser limit for single-junction solar cells a high absorption coefficient (~ 10^5 cm^{-1}), and adequate carrier mobility (>10 $cm^2/V\cdot s$) [5]. Moreover, its fully inorganic structure enhances thermal stability and allows low-temperature solution processing, making it compatible with scalable and flexible device architectures [6].However, the practical application of $CsSnI_3$ remains challenged by poor ambient stability, primarily due to the oxidation of Sn^{2+} to Sn^{4+}. This redox instability introduces deep-level defects that severely reduce carrier lifetimes and compromise device performance [7]. Additionally, $CsSnI_3$ exhibits intrinsic p-type conductivity and self-compensating defects, which complicate doping control and lead to inconsistencies in device fabrication and operation [8].

Recent advances have targeted these challenges through material and interface engineering. For instance, Jung et al. demonstrated that tailored interfacial modifications can enhance device efficiencies to over 8%, underscoring the critical role of interface quality in performance optimization [9]. Complementary computational studies such as those by Umama et al. using SCAPS-1D simulations have highlighted the sensitivity of device behavior to absorber doping levels, defect densities, and multilayer architecture design [10]. Tao et al. further emphasized the importance of energy level alignment and defect passivation to suppress non-radiative recombination and improve operational stability [11].

In this work, we present a systematic SCAPS-1D numerical optimization of ZnO:Al/PCBM/$CsSnI_3$/MoO_3 lead-free perovskite solar cells. The effects of absorber and transport layer thickness, doping concentration, defect density, series and shunt resistances, and operating temperature on photovoltaic performance are investigated. The study aims to identify key loss mechanisms and establish realistic design guidelines for achieving high-efficiency $CsSnI_3$-based solar cells, while clarifying the gap between theoretical performance limits and experimentally attainable efficiencies.

Motivated by these findings, this work presents a numerical optimization of a planar heterojunction $CsSnI_3$-based solar cell using SCAPS-1D simulation. The proposed device architecture consists of ZnO:Al as the transparent conductive oxide (TCO), PCBM as the electron transport layer (ETL), $CsSnI_3$ as the light-absorbing layer, and MoO_3 as the hole transport layer (HTL). Each material is strategically selected for its synergistic contributions to device performance: ZnO:Al offers high conductivity and transparency [12], PCBM promotes efficient electron extraction and suppresses interfacial recombination [13], $CsSnI_3$ ensures strong light absorption while eliminating toxic lead, and MoO_3 facilitates selective hole collection with superior thermal and chemical stability [14].Through comprehensive parametric analysis, we examine the influence of key physical parameters including absorber thickness, doping concentration, ETL thickness, defect density, series resistance (R_S), shunt resistance (R_{SH}), and operating temperature on photovoltaic performance metrics such as open-circuit voltage (V_{oc}), short-circuit current density (J_{sc}), fill factor (FF), and overall power conversion efficiency (PCE). The study aims to identify key loss mechanisms and establish realistic design guidelines for achieving high-efficiency $CsSnI_3$-based solar cells, while clarifying the gap between theoretical performance limits and experimentally attainable efficiencies.

2. Material and Methods

This study employs numerical simulations of the proposed solar cell (Figure 1a) using the SCAPS-1D software developed by Ghent University, which is widely used for modeling thin-film and perovskite solar cells [15]. The simulator self-consistently solves the fundamental semiconductor equations, including [10,16] ;

Poisson's equation:

$$\frac{d^2\psi(x)}{dx^2} = -\frac{q}{\varepsilon}p(x) - n(x) + N_D^+(x) - N_A^-(x) \quad (1)$$

$\psi(x)$ is the electrostatic potential across the device, q is the elementary charge, ε is the permittivity, $n(x)$ and $p(x)$ are the electron and hole densities, and $N_D^+(x)$, $N_A^-(x)$ are the ionized donor and acceptor concentrations.

Electron and Hole continuity equations:

$$\frac{dn(x)}{dt} = \frac{1}{q}\frac{dJ_n(x)}{dx} + G(x) - R(x) \quad (2)$$

$$\frac{dp(x)}{dt} = -\frac{1}{q}\frac{dJ_p(x)}{dx} + G(x) - R(x) \quad (3)$$

where $\frac{dn(x)}{dt}$ and $\frac{dp(x)}{dt}$ are the time-dependent changes in electron and hole concentrations, respectively. $J_n(x)$ and $J_p(x)$ are the electron and hole current densities, $G(x)$ is the generation rate, and $R(x)$ is the recombination rate.

Drift-diffusion current equations:

$$J_n = qn\mu_n E + qD_n\frac{dn}{dx} \quad (4)$$

$$J_p = qp\mu_p E - qD_p\frac{dp}{dx} \quad (5)$$

where J is the total current density, μ is the carrier mobility, E is the electric field, and D is the diffusion coefficient for electrons (n) and holes (p).These equations describe the electrostatic potential, charge carrier transport, generation, and recombination processes within the device. By solving them under both illuminated and dark conditions, SCAPS-1D enables the evaluation of the internal electric field, carrier distribution, and overall photovoltaic performance [17].

In the investigated solar cell (Figure 1a), the TCO (ZnO:Al) collects electrons while efficiently transmitting incident light due to its wide bandgap (3.429 eV) and high electrical conductivity [18,19]. The ETL (PCBM), a fullerene derivative, facilitates selective electron extraction and blocks holes, while providing favorable energy level alignment with the absorber layer [20,21]. The absorber layer ($CsSnI_3$), a lead-free tin-based perovskite, serves as the primary photon-absorbing and charge-generating layer owing to its direct bandgap (1.3 eV) and high charge carrier mobility [10,22]. The HTL (MoO_3) exhibits a wide bandgap (3 eV), high electronegativity, and high dielectric permittivity, enabling efficient hole extraction and electron blocking, while ensuring optimal valence band alignment with the absorber [23]. The back electrode, typically made of a noble metal such as silver (Ag) or gold (Au), collects holes and completes the external circuit.The energy levels presented in Figure 1(a) show that the conduction band edge decreases progressively from ZnO:Al (- 4.2 eV) to PCBM (- 3.7 eV) and then remains nearly constant within $CsSnI_3$, thereby facilitating electron transport [24]. Conversely, the valence band edge increases significantly from MoO_3 (- 9.7 eV) to $CsSnI_3$ (- 5.5 eV), which promotes efficient hole transport [25]. The p-n junction is established within the $CsSnI_3$ absorber layer, with the Fermi level positioned around - 3.7 eV, indicating favorable energy alignment for efficient separation of photogenerated charge carriers [10]. This configuration ensures optimal energy level matching among all constituent materials, which is crucial for minimizing recombination losses and enhancing the overall performance of the solar cell.Table 1 summarizes the parameters of our $CsSnI_3$-cell solar used in the simulation before performance optimization. Note that in this table, the bulk defect density of the $CsSnI_3$ absorber was initially assumed to be on the order of 10^{12} cm^{-3}, representing an idealized yet physically attainable scenario. Although tin-based perovskites are inherently susceptible to elevated defect densities arising from the oxidation of Sn^{2+} to Sn^{4+} and the associated formation of deep-level trap states, recent experimental advances have demonstrated that such defect densities can be substantially mitigated. In particular, the implementation of chemical passivation strategies [26], additive engineering, and strict control of processing conditions has been shown to suppress non-radiative recombination centers [27], [28], yielding trap densities approaching 10^{12} - 10^{13} cm^{-3} in high-quality $CsSnI_3$ films. Accordingly, the adopted defect density may be regarded as a lower-bound estimate corresponding to optimized material quality.

The vacuum-level band diagram presented in Figure 1(b) suggests a large valence band offset at the $CsSnI_3/MoO_3$ interface, Fermi-level equilibration [29], strong band bending within the absorber, and the formation of interface dipoles substantially reduce the effective hole extraction barrier. As a result, MoO_3 functions as an efficient hole-selective contact with a high work function [30], enabling hole collection via field-assisted transport and tunneling mechanisms. These interfacial effects account for the high device performance despite the apparently large valence band offset.

In our simulations, both the front and back contacts are assumed to be ideal (ohmic). The reference temperature is set to 300 K, except for the thermal stability analysis. All calculations were performed under standard AM1.5G illumination with an irradiance of 1000 $W \cdot m^{-2}$ [31]. The photovoltaic performance of the solar cell was evaluated in terms of the open-circuit voltage (V_{oc}), short-circuit current density (Jsc), fill factor (FF), and power conversion efficiency (PCE), defined as follows:

$$PCE = \frac{V_{oc} \cdot J_{sc} \cdot FF}{P_{in}} \tag{4}$$

$$FF = \frac{P_{max}}{V_{oc} \cdot J_{sc}} = \frac{V_{mp} \cdot J_{mp}}{V_{oc} \cdot J_{sc}} \tag{5}$$

V_{mp} and J_{mp} are the voltage and current density at the maximum power point, P_{in} is the incident solar power density, typically 100 mW/cm² under AM1.5G illumination.The J-V characteristic curve (Figure 1(c)) and the external quantum efficiency spectrum curve QE(λ) (Figure 1(d)) were obtained by a SCAPS simulation of our initial structure. These results demonstrate efficient charge generation and extraction within the device architecture on the one hand, and excellent light absorption and optimal charge collection efficiency in the visible range on the other [32]. In particular, we obtained the following values: J_{sc} = 31.16 mA/cm², V_{oc} = 0.8662 V, FF = 80.14%, and PCE = 21.63%, which are consistent with the literature [32-33].The optimization of the proposed solar cell is carried out in the following section by varying in particular some parameters of the $CsSnI_3$ and PCBM layers.

3. Results and Discussions

3.1 Effect of $CsSnI_3$ and PCBM layer thickness

Figures 2 and 3 illustrate the influence of the $CsSnI_3$

Table 1. *Input parameters used in the simulation* [32,34,35]

Parameters	**ZnO:AL**	**PCBM**	**$CsSnI_3$**	**MoO_3**
Thickness (µm)	0.05	0.05	0.4	0.4
Band gap, E_g (eV)	3.429	2	1.3	3
Electron affinity, χ (eV)	3.99	3.9	3.6	2
Dielectric relative permittivity, ε_r	9	3.9	9.93	35
CB effective density of states, N_C (cm^{-3})	6.040×10^{18}	2.5×10^{21}	1.75×10^{19}	2.42×10^{19}
VB effective density of states, N_V (cm^{-3})	4.476×10^{19}	2.5×10^{21}	1.47×10^{18}	2.42×10^{19}
Electron mobility, μ_n (cm^2/Vs)	85	2×10^{-1}	50	50
Hole mobility, μ_h (cm^2/Vs)	70	2×10^{-1}	5.85×10^{2}	50
Shallow uniform acceptor density,N_a (cm^{-3})	0	0	10^{19}	10^{17}
Shallow uniform donor density, N_d (cm^{-3})	1.3×10^{16}	2.93×10^{17}	0	0
Defect density, N_t (cm^{-3})	10^{15}	10^{15}	10^{12}	10^{15}

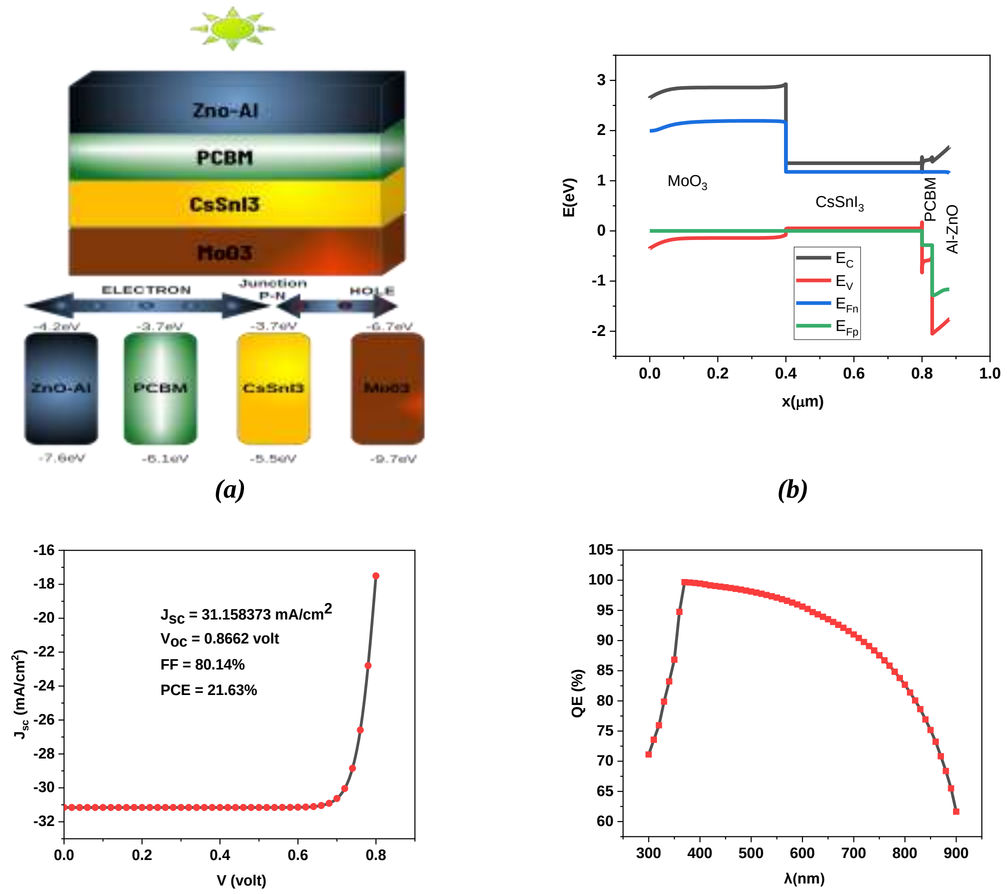

(a) *(b)*

(c) *(d)*

Figure 1. *(a) Energy level diagram of the studied solar cell, (b) energy band diagram, (c) current density-voltage (J-V) characteristic, (d) external quantum efficiency (QE) as a function of wavelength (λ)*

absorber and PCBM layer thicknesses on the photovoltaic performance of the device. The $CsSnI_3$ thickness was varied from 0.2 to 1.2 µm, while the PCBM thickness ranged from 0.1 to 0.5 µm; all other device parameters were kept constant.As shown in Figure 2, increasing the $CsSnI_3$ thickness results in a pronounced enhancement of the short-circuit current density (Jsc) and power conversion efficiency (PCE), which increase from 24.86 to 35.05 $mA \cdot cm^{-2}$ and from 17.7% to 23.36%, respectively, owing to improved light absorption. In contrast, the open-circuit voltage (Voc) exhibits a slight decrease from 0.914 V to 0.834 V, which is attributed to increased bulk recombination in thicker absorber layers. The enhancement in Jsc and PCE saturates beyond approximately 0.8 µm, indicating diminishing performance gains with further thickness increase. The fill factor (FF) improves with increasing absorber thickness, reaching a maximum value of 80.44% at 0.6 µm, before slightly declining due to enhanced recombination losses and increased internal resistance. These results suggest an optimal $CsSnI_3$ thickness of 1.2 µm, yielding a PCE of 23.36% and an FF of 79.88%, in good agreement with previously reported trends for $CsSnI_3$-based solar cells [36-38].

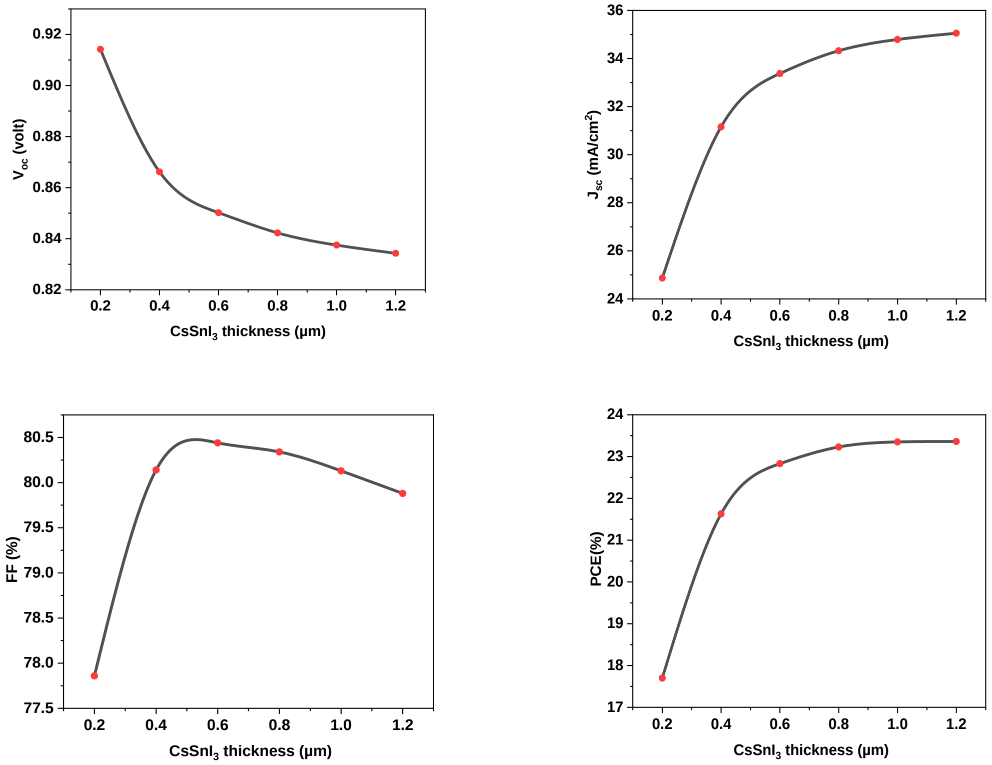

Figure 2. *Evolution of Jsc, Voc, FF, and PCE as a function of CsSnI$_3$ layer thickness*

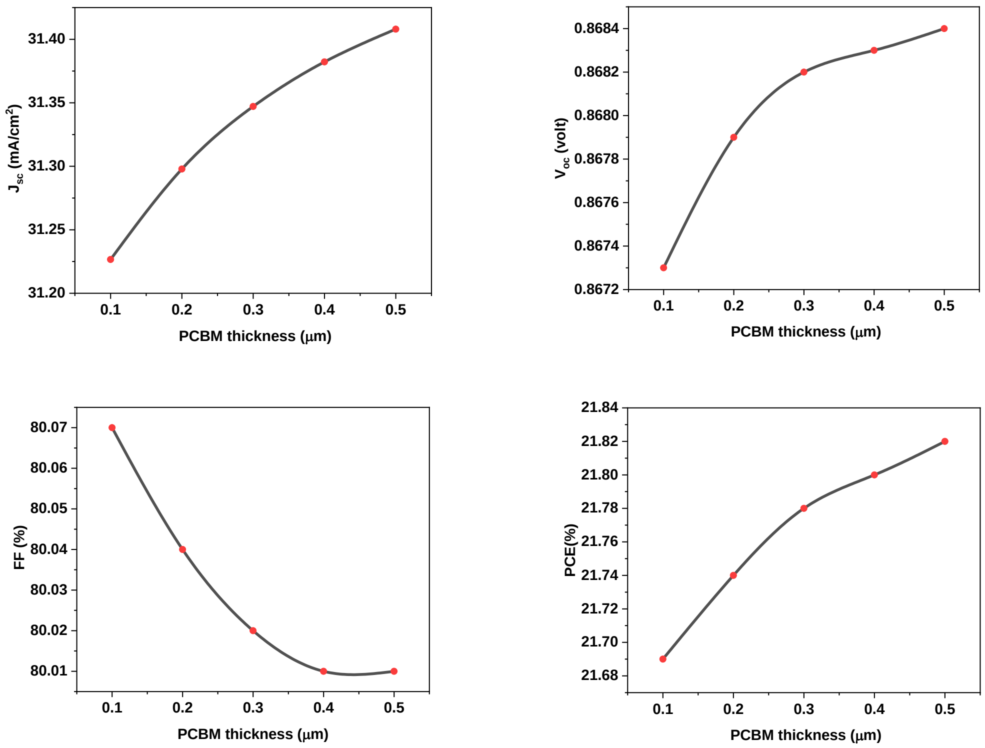

Figure 3. *Evolution of Jsc, Voc, FF, and PCE as a function of PCBM layer thickness*

Figure 3 indicates that the PCBM thickness has a relatively minor impact on device performance. An optimal PCBM thickness of 0.5 μm results in a PCE of 21.82%, while thinner PCBM layers (~0.1 μm) do not significantly degrade the photovoltaic parameters, in agreement with previous studies [37].

3.2 Effect of CsSnI$_3$ and PCBM doping concentration

Doping is a key strategy for controlling charge carrier concentration, electrical conductivity, and Fermi level position in solar cell layers. Figures 4 and 5 present the influence of acceptor (N_a) and donor (N_d) doping concentrations in the $CsSnI_3$ absorber and PCBM layers, respectively, varied from 10^{14} to 10^{19} cm^{-3}, while all other parameters were kept constant.

It shoud be noted that the $CsSnI_3$ absorber layer was intentionally doped up to high acceptor concentrations (~10^{19} cm^{-3}) to evaluate the upper performance limits associated with strong p-type conductivity, which is physically plausible in tin-based perovskites due to intrinsic self-doping and tin-vacancy formation [39,40]. To isolate the effect of doping, the defect density was fixed at a low value (10^{12} cm^{-3}), minimizing recombination losses. While this represents an idealized scenario, it provides insight into the maximum achievable device performance, although moderate doping levels may be more practical experimentally.

As shown in Figure 4, V_{oc} and J_{sc} remain nearly unchanged up to 10^{16} cm^{-3}, followed by a slight increase from 0.806 to 0.833 V and from 35.02 to 35.05 mA cm^{-2}, respectively. In contrast, PCE and FF increase more noticeably, rising from 16.9% to 23.36% and from 59.77% to 79.88%. This improvement is attributed to the enhanced internal electric field and built-in potential, which promote efficient charge separation and extraction. An optimal acceptor concentration of 10^{19} cm^{-3} is identified, offering a favorable balance between improved carrier collection and limited recombination.

Figure 5 shows that variations in the donor concentration of the PCBM layer have a negligible impact on photovoltaic performance. This behavior is expected, as transport layers do not participate in photogeneration but primarily facilitate selective carrier extraction. Once sufficient conductivity and energy-level alignment are achieved, further doping provides little benefit, particularly for thin layers where carrier transport is already efficient [36].

3.3 Effect of $CsSnI_3$ and PCBM defect densities

Figure 6 shows the evolution of J_{sc}, V_{oc}, FF, and PCE as a function of defect density (N_t) in the $CsSnI_3$ and PCBM layers.

An increase in $CsSnI_3$ defect density leads to a systematic reduction in device performance. In particular, V_{oc} decreases monotonically with increasing N_t, indicating enhanced Shockley-Read-Hall (SRH) recombination via deep trap states in the absorber. While J_{sc} remains nearly unchanged at low defect densities, a noticeable decline occurs at higher N_t due to reduced carrier diffusion length and incomplete charge collection. The FF exhibits an initial improvement followed by degradation at high defect densities, reflecting the competition between improved transport and increased recombination losses. Consequently, the PCE decreases continuously, confirming that bulk defects in $CsSnI_3$ dominate the recombination dynamics.

In contrast, the impact of PCBM defect density on device performance is comparatively weaker. A moderate increase in N_t slightly enhances V_{oc}, which can be attributed to improved band bending and reduced interfacial recombination at the PCBM/$CsSnI_3$ junction. However, excessive defect density degrades J_{sc} and FF due to trap-assisted recombination and reduced electron mobility. Overall, the PCE shows only minor variation, indicating that the electron transport layer (ETL) is more defect-tolerant than the absorber layer.

These results demonstrate that defect passivation in the $CsSnI_3$ absorber is a key factor for achieving high-efficiency, lead-free perovskite solar cells, whereas moderate defect densities in the PCBM layer can be tolerated without significant efficiency loss.

3.4 Effects of Series and Shunt Resistances

Series (R_S) and shunt (R_{SH}) resistances critically influence photovoltaic device performance by governing ohmic losses and leakage currents, respectively. Figures 6 and 7 illustrate their effects on the solar cell parameters. R_S was varied from 1 to 6 Ω·cm² with RSH fixed at 10^2 Ω·cm², while R_{SH} was varied from 10 to 10^6 Ω·cm² with RS set to 0 Ω·cm². All other parameters were kept constant.

As shown in Figure 7, increasing R_S leads to a pronounced degradation of device performance. FF decreases linearly from 77% to 60% due to enhanced ohmic losses, which reduce the maximum extractable power. J_{sc} shows a marginal decrease from 31.1581 to 31.1573 mA/cm², reflecting the limited impact of R_S on current generation. In contrast, V_{oc} remains nearly constant at 0.81 V, as it is primarily governed by recombination processes rather than series resistance [41,42]. Consequently, PCE drops from 20.75% to 16.3%. These results highlight the necessity of minimizing R_S to reduce power losses and avoid excessive heat dissipation.

Figure 8 presents the impact of R_{SH} on device performance. With increasing R_{SH}, J_{sc} remains

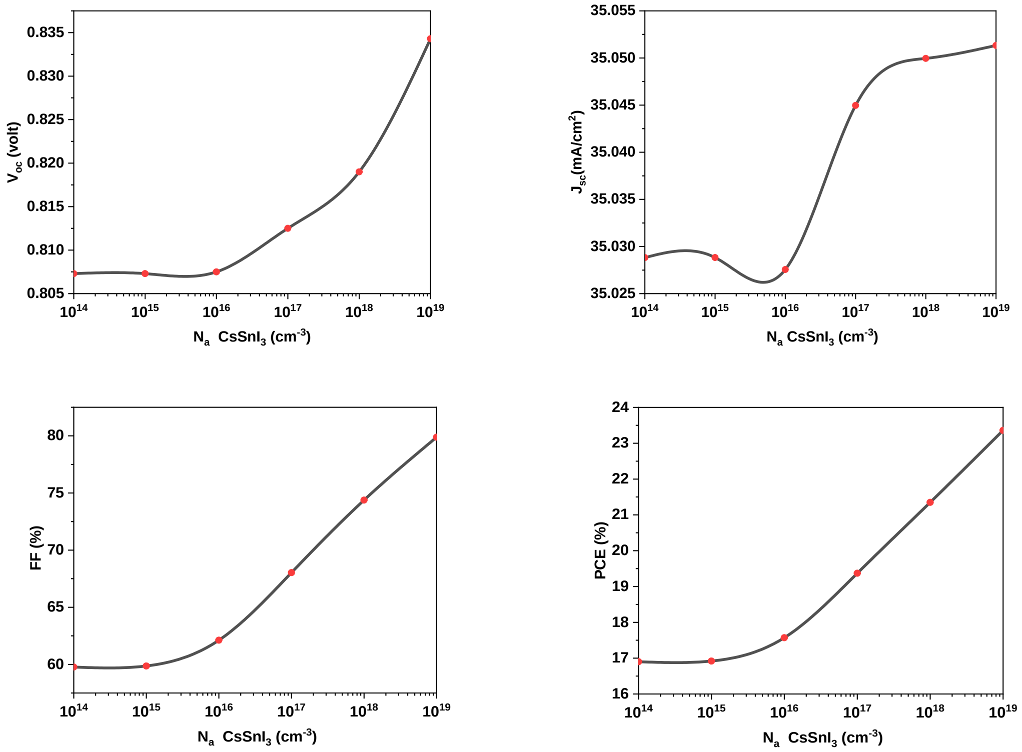

Figure 4. *Evolution of J_{sc}, V_{oc}, FF, and PCE as a function of CsSnI$_3$ layer doping concentration (N_a)*

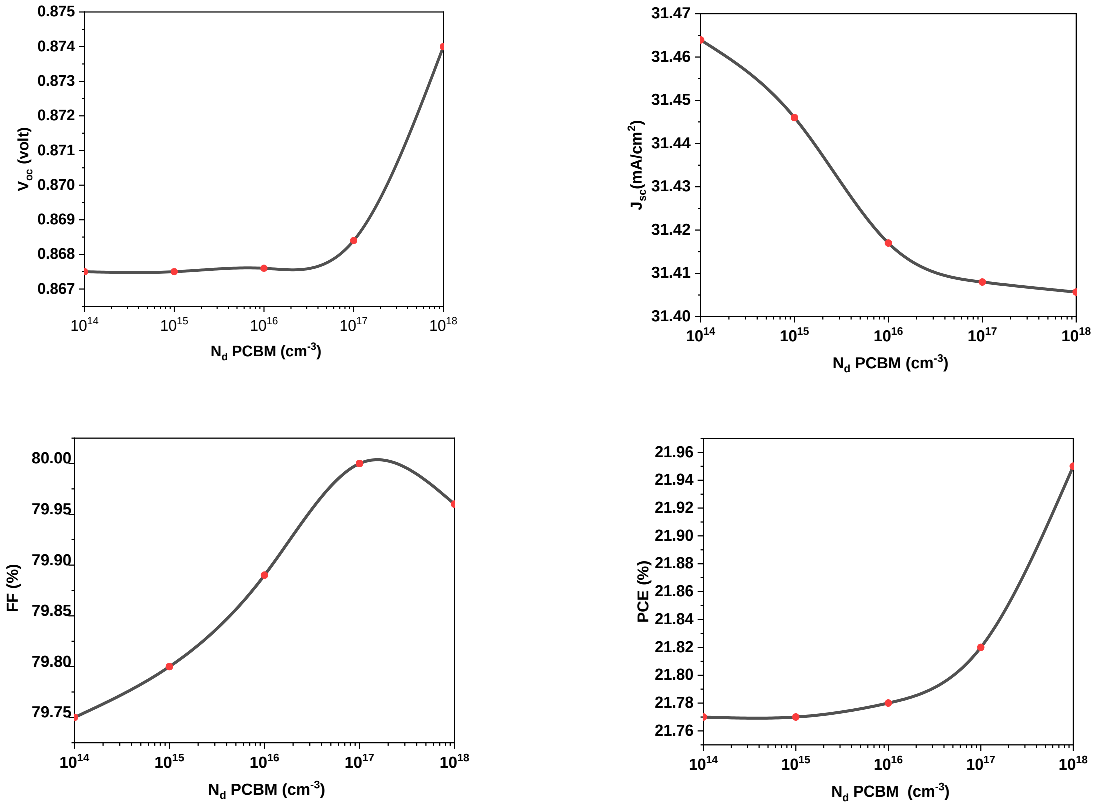

Figure 5. *Evolution of J_{sc}, V_{oc}, FF, and PCE as a function of PCBM layer doping concentration (N_d)*

almost unchanged at ~31.15 mA/cm², confirming that photogenerated current is weakly affected by leakage pathways. However, significant improvements are observed in V_{oc}, FF, and PCE as R_{SH} increases, particularly below 10^4 Ω·cm². V_{oc} increases from 0.31 to 0.86 V, while FF and PCE rise from 25% to 80% and from 2.5% to 22%, respectively. These enhancements result from the suppression of leakage currents, which allows better charge collection and improved junction

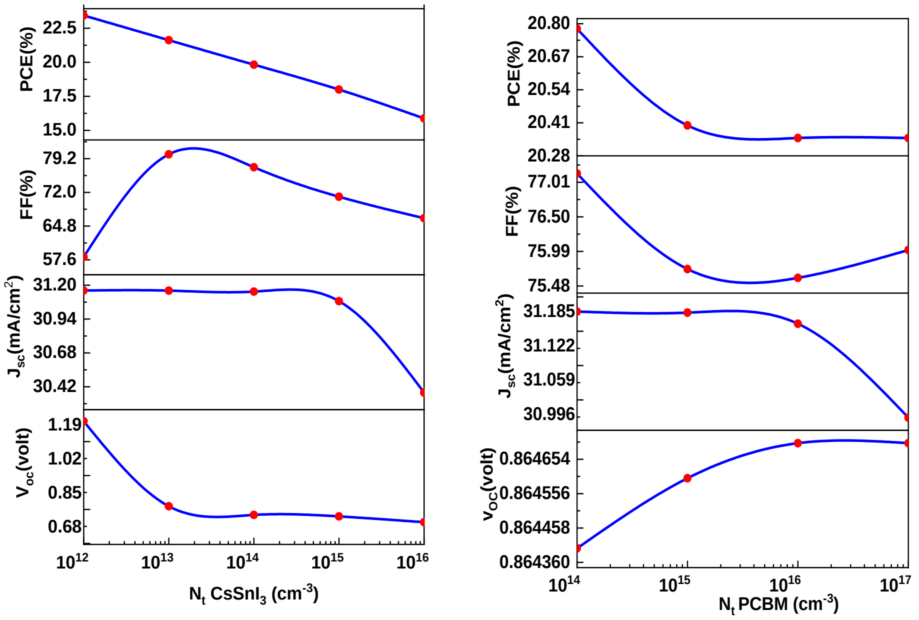

***Figure 6**. Evolution of J_{sc}, V_{oc}, FF, and PCE as a function of $CsSnI_3$ and PCBM layer defect density (N_t)*

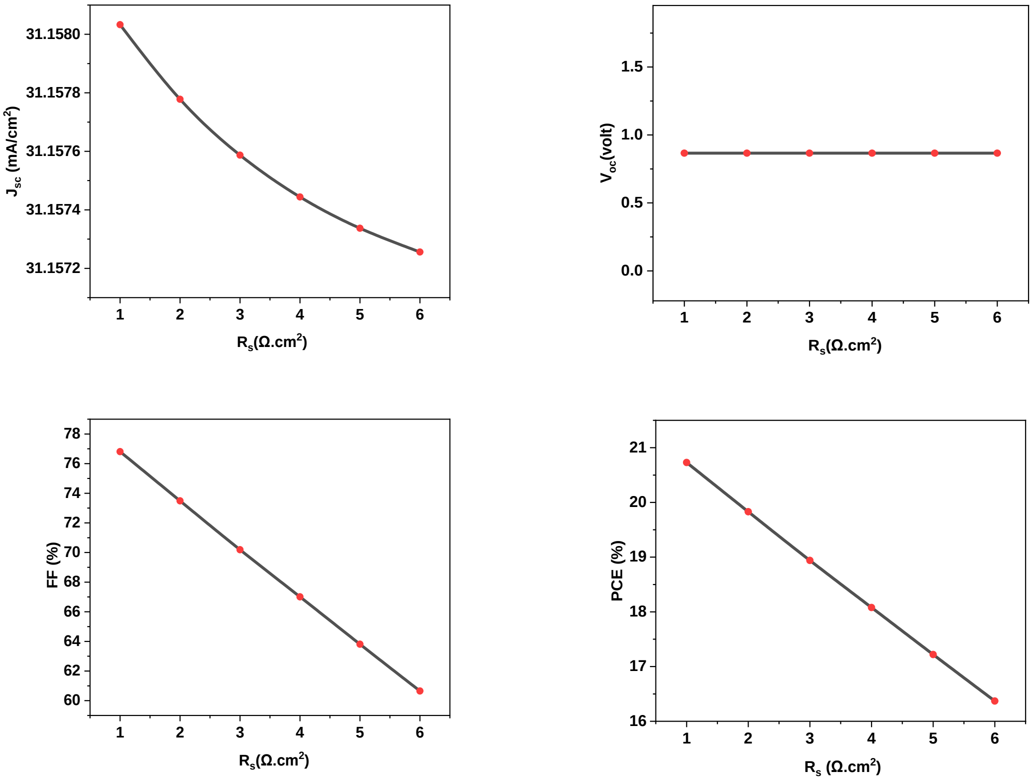

***Figure 7.** Effect of Series Resistance (R_S) on J_{sc}, V_{oc}, FF, and PCE with fixed Shunt Resistance (R_{SH} = 10^2 Ω·cm²)*

potential [32]. Beyond 10^4 Ω·cm², performance parameters tend to saturate.

Overall, optimal device performance requires low series resistance to ensure efficient charge transport and high shunt resistance to suppress leakage currents and preserve photogenerated carriers.

3.5 Effect of temperature

Figure 9 presents the evolution of J_{sc}, V_{oc}, FF, and PCE as a function of temperature. As temperature increases, the open-circuit voltage (V_{oc}) exhibits a clear upward trend. This behavior can be attributed to enhanced carrier activation and improved band

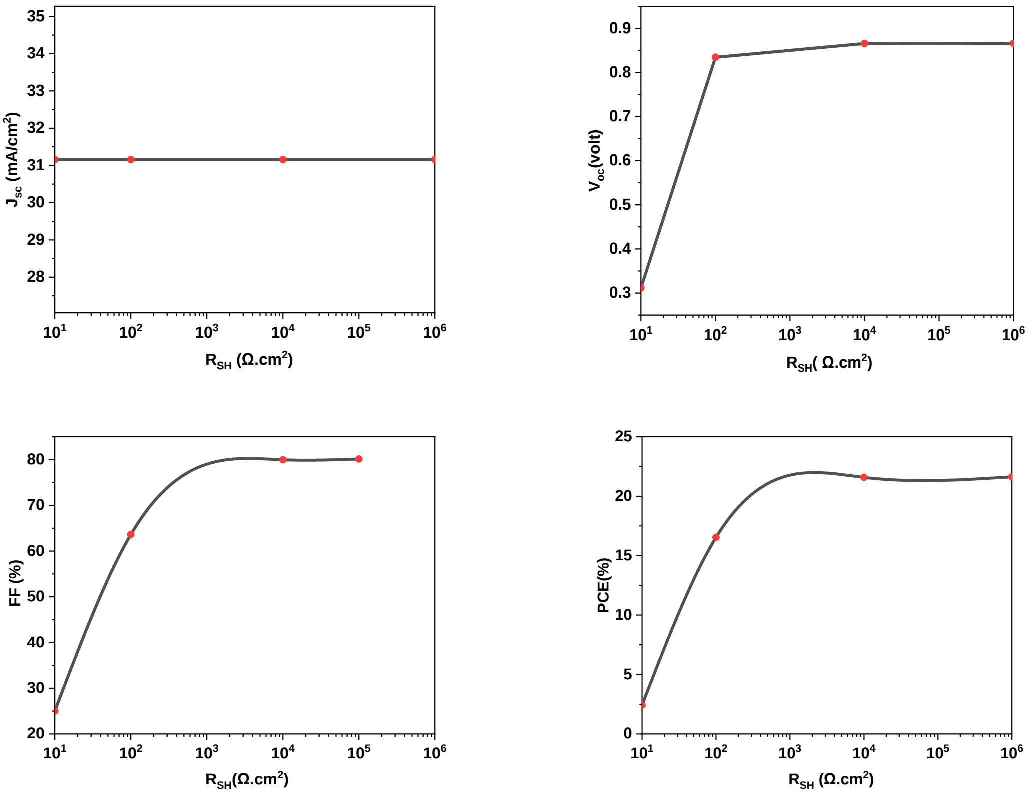

Figure 8. *Effect of Shunt Resistance (R_{SH}) on J_{sc}, V_{oc}, FF, and PCE with fixed Series Resistance (R_S = 0 Ω·cm²)*

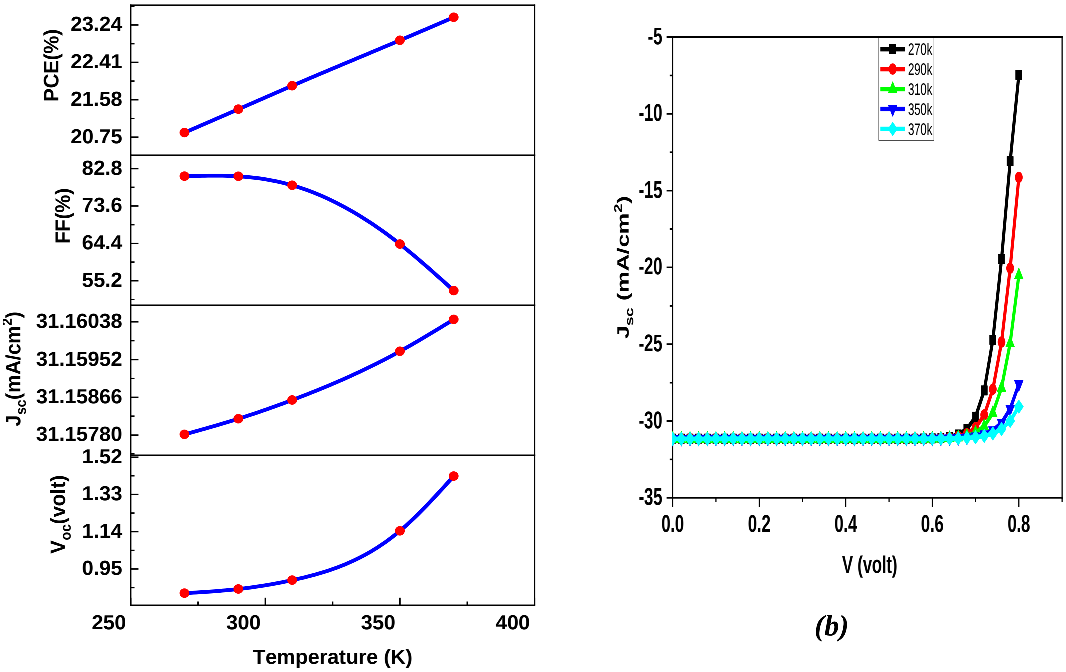

(b)

(a)

Figure 9. *(a) Evolution of J_{sc}, V_{oc}, FF, and PCE as a function of temperature. (b) Simulated J–V characteristic curves at different temperatures*

bending at the heterointerfaces, which facilitate charge separation and extraction under illumination. In SCAPS-1D, temperature-dependent carrier statistics and reduced interfacial recombination can jointly contribute to this increase. The short-circuit current density (J_{sc}) increases moderately with temperature, reflecting improved carrier mobility and thermally assisted transport across interfaces. Enhanced diffusion and reduced transport barriers enable more efficient charge collection at elevated temperatures. In contrast, the fill factor (FF) decreases monotonically with temperature. This degradation is primarily associated with increased series resistance, higher phonon scattering, and enhanced recombination losses, which distort the current–voltage characteristics near the maximum power point. Despite the FF reduction, the power conversion efficiency (PCE) increases with temperature, indicating that the combined gains in V_{oc} and J_{sc} outweigh the FF losses within the investigated temperature range. This result suggests good thermal tolerance of the ZnO:Al/PCBM/$CsSnI_3$/MoO_3 architecture, a favorable attribute for practical operating conditions. Overall, the device performance is governed by a competition between thermally enhanced carrier transport and temperature-induced resistive and recombination losses.

3.6 Effect of Temperature on Series and Shunt Resistances

Understanding the temperature dependence of series (R_S) and shunt (R_{SH}) resistances is essential for evaluating device stability under operating conditions. Figure 10 shows that V_{oc} remains nearly independent of R_S, with a slight increase at higher temperatures, likely due to thermally activated carriers. In contrast, the FF decreases with temperature, indicating increased recombination, phonon scattering, and effective resistive losses. Although the PCE decreases with temperature, higher temperatures yield slightly higher PCE at a fixed R_S, suggesting improved material conductivity partially compensates resistive losses. The J_{sc} increases marginally with temperature, consistent with thermally assisted carrier transport and bandgap narrowing.

Figure 11 illustrates the effect of R_{SH} on device performance. J_{sc} remains nearly constant, while V_{oc} and PCE improve significantly with increasing R_{SH}, particularly at elevated temperatures. High R_{SH} suppresses leakage currents, enabling higher voltages and efficiencies. FF increases with R_{SH} at low temperatures but slightly degrades at high temperatures due to competing resistive and transport losses. Maximum efficiencies of ~23.5% are achieved for $R_{SH} > 10^4\ \Omega\cdot cm^2$.

Overall, $CsSnI_3$-based devices exhibit good thermal robustness, maintaining competitive performance at elevated temperatures. However, minimizing R_S and maximizing R_{SH} through optimized contacts, interface engineering, and encapsulation remain crucial to mitigating thermal degradation and ensuring long-term operational stability [32,43-46].

Table 2 presents a comparison of the photovoltaic parameters of $CsSnI_3$-based solar cells obtained from recent experimental studies and simulation and of the optimized device simulated in this work.

As shown in Table 2, experimentally reported power conversion efficiencies for single-junction $CsSnI_3$ devices typically range from 7 % to approximately 23 %, depending on interface engineering, charge transport layers, and defect passivation strategies [47,48,49].

Higher efficiencies exceeding 25 % are mainly associated with simulation studies or idealized device configurations, where assumptions such as low bulk and interfacial defect densities, ideal energy-level alignment, and ohmic contacts are employed. In contrast, practical devices are limited by Sn^{2+} oxidation, interfacial recombination, and contact resistance, which lead to reduced open-circuit voltage, fill factor, and overall efficiency [50].

Therefore, the simulation results reported in this work should be regarded as theoretical upper-limit performance, illustrating the potential efficiency enhancement achievable through effective defect passivation and optimized interface design, rather than as directly attainable experimental values. The good agreement between simulated trends and experimentally reported data confirms the physical validity of the model while maintaining a realistic interpretation of device performance.

The optimized solar cell achieved a power conversion efficiency of 25.39%, with V_{oc} = 0.9743 V, J_{sc} = 35.05 $mA\cdot cm^{-2}$, and FF = 74.34%, values that are comparable to or exceed those reported in recent literature (Table 2). The corresponding current-voltage (J-V) characteristics and external quantum efficiency (QE) spectra as a function of wavelength (λ) for the optimized device are presented in Figure 12, demonstrating efficient light absorption across the visible spectrum and effective charge extraction, consistent with the observed improvements in photovoltaic performance.

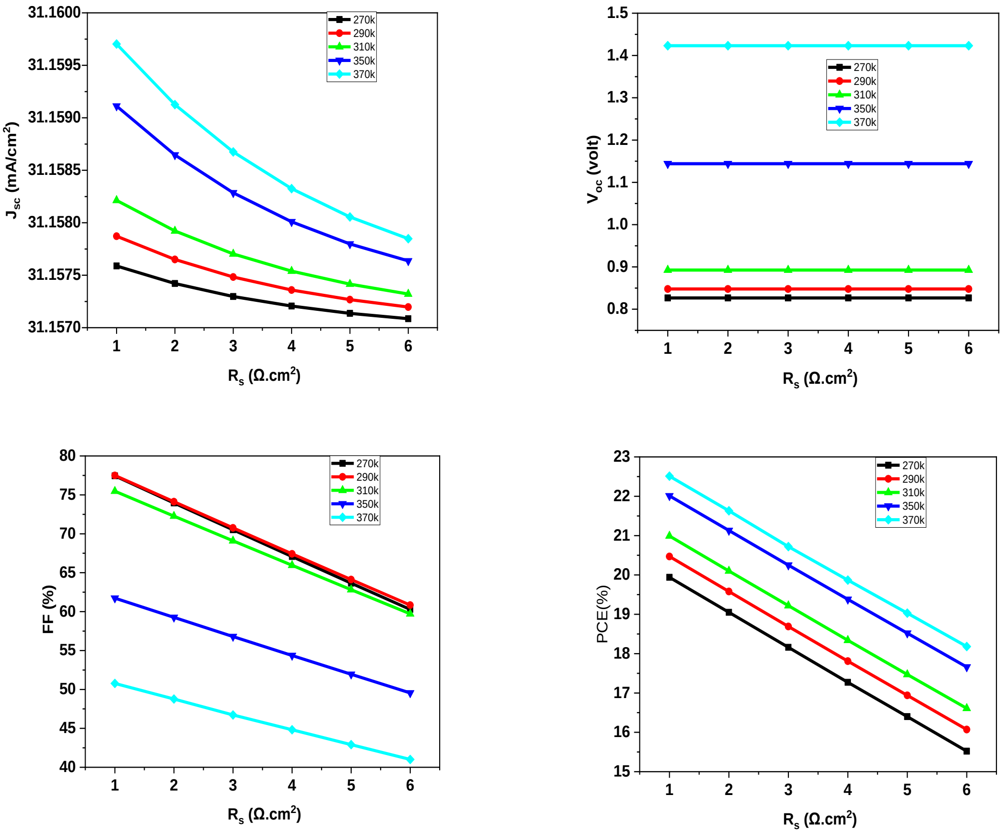

Figure 10. *Effect of temperature on Series Resistance R_S and overall performance parameters of studied $CsSnI_3$ Solar Cell*

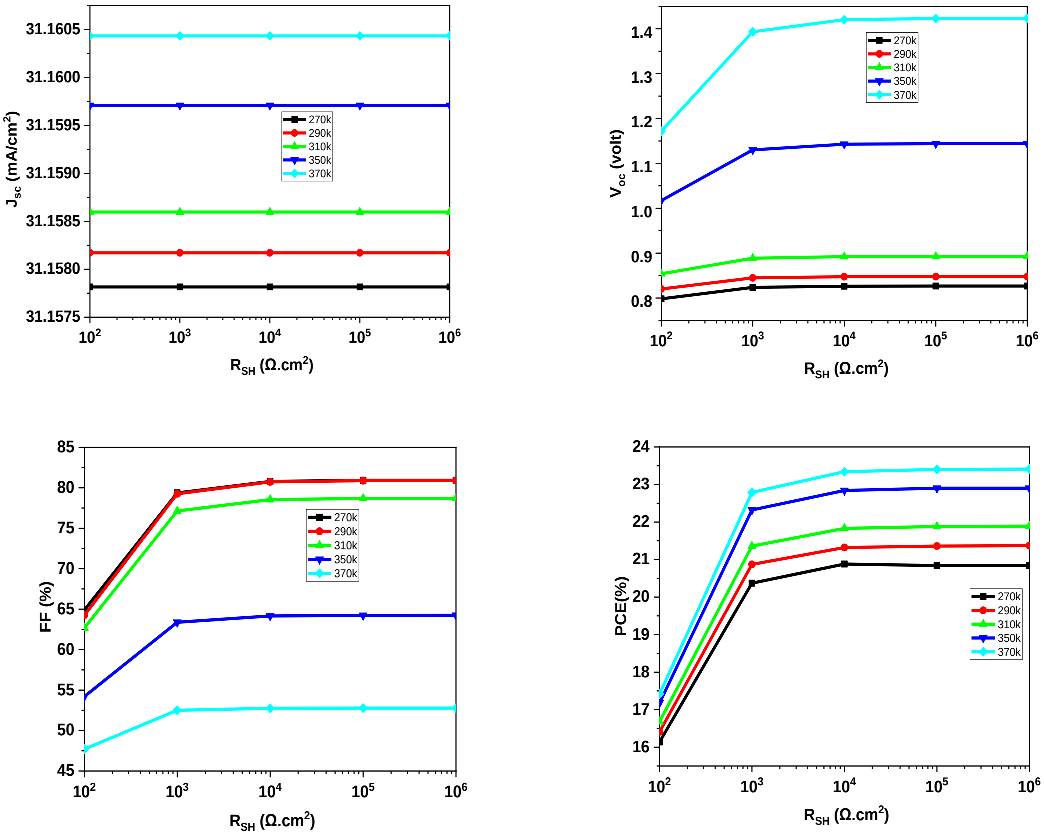

Figure 11. *Effect of temperature on Shunt Resistance R_{SH} and overall performance parameters of studied $CsSnI_3$ Solar Cell*

Table 2. *Comparison of photovoltaic parameters of $CsSnI_3$-based solar cells reported in the literature and the optimized device simulated in this work*

Device architecture	V_{oc} (V)	J_{sc} ($mA.cm^{-2}$)	FF(%)	PCE(%)	Ref.
FTO /PEDOT:PSS/$CsSnI_3$	1.143	24.25	72.1	20.96	[51] (exp.)
FTO /PEDOT:PSS/TSBCNT-$CsSnI_3$	1.174	24.90	79.5	23.34	[51] (exp.)
FTO/TIO2/P3HT/$CsSnI_3$(MBAA)	0,45	24.85	67	7.5	[52] (exp.)
ITO/PEDOT:PSS/CsSnI3/ICBA/BCP/Ag	0.77	22.68	69	12.05	[53] (exp.)
ITO/PCBM/$CsSnI_3$/CFTS/Se	1.141	15.10	58.50	24.73	[54] (Sim.)
ITO/ZnSe/$CsPbI_3$/ $CsSnI_3$	2.245	14.673	89.20	29.38	[55] (Sim.)
Top_MXene electrode / $CsSnI_{3-x}Br_x$/bottom_MXene electrode	1.20	28.7	85	29.3	[56] (Sim.)
ZnO:Al/PCBM/$CsSnI_3$/MoO_3	0.9743	35.052	74.34	25.39	Our work (Sim.)

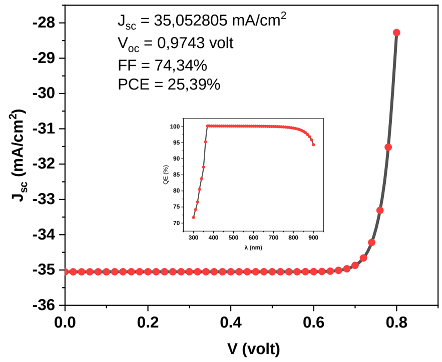

Figure 12. *Current density-voltage (J-V) characteristics and external quantum efficiency (QE) as a function of wavelength (λ) for the optimized $CsSnI_3$ solar cell*

4. Conclusions

The photovoltaic performance of ZnO:Al/PCBM/$CsSnI_3$/MoO_3 solar cells was numerically optimized using SCAPS-1D. The study demonstrates that the $CsSnI_3$ absorber layer governs device efficiency through its thickness, doping level, and defect density. Increasing absorber thickness enhances light absorption and current density, with efficiency saturation beyond ~1 µm due to recombination. High p-type doping improves the fill factor and power conversion efficiency by strengthening the built-in electric field, whereas PCBM properties have a minor influence. Defect density in $CsSnI_3$ is identified as the primary recombination source, highlighting the critical role of bulk and interface defect passivation. Device performance is highly sensitive to series and shunt resistances, emphasizing the importance of contact optimization. Temperature-dependent analysis indicates good thermal tolerance of the proposed architecture. An optimized efficiency of 25.39% is achieved under idealized conditions, consistent with recent simulation studies. Although experimental performance remains limited by tin oxidation and contact losses, the results provide practical design guidelines for advancing high-efficiency, lead-free $CsSnI_3$-based perovskite solar cells.

Author Statements:

- **Ethical approval:** The conducted research is not related to either human or animal use.
- **Conflict of interest:** The authors declare that they have no known competing financial interests or personal relationships that could have appeared to influence the work reported in this paper.
- **Acknowledgement:** The authors would like to thank the Laboratory of Physico-Chemistry of Materials and Environment (LPCME), at Ziane Achour University, Djelfa, Algeria, and the Algerian General Directorate of Scientific Research and Technological Development (DGRSDT) for their academic and scientific support.
- **Author contributions:** The authors declare that they have equal right on this paper.
- **Funding information:** The authors declare that there is no funding to be acknowledged.
- **Data availability statement:** The data that support the findings of this study are available on request from the corresponding author. The data are not publicly available due to privacy or ethical restrictions.

References

[1] National Renewable Energy Laboratory. (n.d.). *Best research-cell efficiencies.* https://www.nrel.gov/pv/cell-efficiency

[2] Kojima, A., Teshima, K., Shirai, Y., & Miyasaka, T. (2009). Organometal halide perovskites as visible-light sensitizers for photovoltaic cells. *Journal of the American Chemical Society*, *131*(17), 6050–6051. https://doi.org/10.1021/ja809598r

[3] Babayigit, A., Ethirajan, A., Müller, M., & Conings, B. (2016). Toxicity of organometal halide perovskite solar cells. *Nature Materials*, *15*(3), 247–251. https://doi.org/10.1038/nmat4572

[4] Hao, F., Stoumpos, C. C., Chang, R. P. H., & Kanatzidis, M. G. (2014). Anomalous band gap behavior in mixed Sn and Pb perovskites enables broadening of absorption spectrum in solar cells. *Journal of the American Chemical Society*, *136*(22), 8094–8099. https://doi.org/10.1021/ja5033259

[5] Stoumpos, C. C., Malliakas, C. D., & Kanatzidis, M. G. (2013). Semiconducting tin and lead iodide perovskites with organic cations: Phase transitions, high mobilities, and near-infrared photoluminescent properties. *Inorganic Chemistry*, *52*(15), 9019–9038. https://doi.org/10.1021/ic401215x

[6] Ye, T., Wang, K., Hou, Y., Yang, D., Smith, N., Magill, B., & Priya, S. (2021). Ambient-air-stable lead-free $CsSnI_3$ solar cells with greater than 7.5% efficiency. *Journal of the American Chemical Society*, *143*(11), 4319–4328. https://doi.org/10.1021/jacs.0c13069

[7] Sabba, D., Mulmudi, H. K., Prabhakar, R. R., Krishnamoorthy, T., Baikie, T., Boix, P. P., & Mathews, N. (2015). Impact of anionic Br substitution on open-circuit voltage in lead-free perovskite ($CH_3NH_3SnI_3{-}xBr_x$) solar cells. *The Journal of Physical Chemistry C*, *119*(4), 1763–1767. https://doi.org/10.1021/jp5126624

[8] Wang, M., Wang, W., Ma, B., Shen, W., Liu, L., Cao, K., & Huang, W. (2021). Lead-free perovskite materials for solar cells. *Nano-Micro Letters*, *13*, 62. https://doi.org/10.1007/s40820-020-00578-z

[9] Lee, H., & Li, D. (2024). Surface passivation to improve the performance of perovskite solar cells. *Energies*, *17*(17), 5282. https://doi.org/10.3390/en17215282

[10] Umama, U. M., Jalal, M. I. E., Siddique, M. A. F., Chowdhury, U., Hoque, M. I. U., & Rahman, M. J. (2025). Simulation and optimization of a $CsSnI_3/CsSnGeI_3/Cs_3Bi_2I_9$ based triple absorber layer perovskite solar cell using SCAPS-1D. *Journal of Physics and Chemistry of Solids*, *198*, 112480. https://doi.org/10.1016/j.jpcs.2024.112480

[11] Tao, S., Schmidt, I., Brocks, G., Jiang, J., Tranca, I., Meerholz, K., & Olthof, S. (2019). Absolute energy level positions in tin- and lead-based halide perovskites. *Nature Communications*, *10*, 2560. https://doi.org/10.1038/s41467-019-10468-7

[12] Lin, M.-L., Huang, J.-M., Ku, C.-S., Lin, C.-M., Lee, H.-Y., & Juang, J.-Y. (2017). High mobility transparent conductive Al-doped ZnO thin films by atomic layer deposition. *Journal of Alloys and Compounds*, *727*, 565–571. https://doi.org/10.1016/j.jallcom.2017.08.207

[13] Liu, M., Johnston, M. B., & Snaith, H. J. (2013). Efficient planar heterojunction perovskite solar cells by vapour deposition. *Nature*, *501*(7467), 395–398. https://doi.org/10.1038/nature12509

[14] Tsai, H., Nie, W., Blancon, J.-C., Stoumpos, C. C., Asadpour, R., Harutyunyan, B., & Mohite, A. D. (2016). High-efficiency two-dimensional Ruddlesden–Popper perovskite solar cells. *Nature*, *536*, 312–316. https://doi.org/10.1038/nature18306

[15] Burgelman, M., Nollet, P., & Degrave, S. (2000). Modelling polycrystalline semiconductor solar cells. *Thin Solid Films*, *361–362*, 527–532. https://doi.org/10.1016/S0040-6090(99)00825-1

[16] Alanazi, T. I., & Eid, O. I. (2023). Simulation of triple-cation perovskite solar cells: Key design factors for efficiency promotion. *Energies*, *16*, 2717. https://doi.org/10.3390/en16062717

[17] Fonash, S. J. (2010). *Solar cell device physics* (2nd ed.). Academic Press. https://doi.org/10.1016/C2009-0-19749-0

[18] Özgür, Ü., Alivov, Y. I., Liu, C., Teke, A., Reshchikov, M. A., Doğan, S., & Morkoç, H. (2005). A comprehensive review of ZnO materials and devices. *Journal of Applied Physics*, *98*(4), 041301. https://doi.org/10.1063/1.1992666

[19] Hosono, H. (2007). Recent progress in transparent oxide semiconductors: Materials and device application. *Thin Solid Films*, *515*, 6000–6014. https://doi.org/10.1016/j.tsf.2006.12.089

[20] Kim, J. Y., Lee, K., Coates, N. E., Moses, D., Nguyen, T.-Q., Dante, M., & Heeger, A. J. (2007). Efficient tandem polymer solar cells fabricated by all-solution processing. *Science*, *317*(5835), 222–225. https://doi.org/10.1126/science.1141711

[21] Snaith, H. J., Abate, A., Ball, J. M., Eperon, G. E., Leijtens, T., Noel, N. K., Stranks, S. D. (2014). Anomalous hysteresis in perovskite solar cells. *The Journal of Physical Chemistry Letters*, *5*, 1511–1515. https://doi.org/10.1021/jz500113x

[22] Fan, Y., Wu, Y., Xu, Y., Li, W., Zhou, H., & Zhang, X. (2022). Situation and perspectives on tin-based perovskite solar cells. *Sustainability*, *14*(24), 16603. https://doi.org/10.3390/su142416603

[23] Davis, R., & P, P. (2021). Aqueous solution-processed tetrasulphonated copper phthalocyanine (TS-CuPc):MoO_3 as an efficient hole transporting layer in organic solar cells. *Materials Science in Semiconductor Processing*, *125*, 105637. https://doi.org/10.1016/j.mssp.2020.105637

[24] Moia, D., & Maier, J. (2023). Ionic and electronic energy diagrams for hybrid perovskite solar cells. *Materials Horizons*, *10*, 1641–1650. https://doi.org/10.1039/d2mh01569b

[25] Zhou, D., Zhou, T., Tian, Y., Zhu, X., & Tu, Y. (2018). Perovskite-based solar cells: Materials, methods, and future perspectives. *Journal of Nanomaterials*, *2018*, Article 8148072. https://doi.org/10.1155/2018/8148072

[26] Li, B., *et al.* (2021). Efficient passivation strategy on Sn-related defects for high-performance all-inorganic $CsSnI_3$ perovskite solar cells. *Advanced Functional Materials*, *31*(11), 2007447. https://doi.org/10.1002/adfm.202007447

[27] Shaikh, A. S., *et al.* (2024). Dynamic synergy of tin in the electron-transfer layer and absorber layer for

advancing perovskite solar cells: A comprehensive review. *Energy Advances*, *3*(7), 1505–1552. https://doi.org/10.1039/d4ya00204k

[28] Wang, G., Chang, J., Bi, J., Lei, M., Wang, C., & Qiao, Q. (2022). Inorganic $CsSnI_3$ perovskite solar cells: Progress and future prospects. *Solar RRL*, *6*(4), 2100841. https://doi.org/10.1002/solr.202100841

[29] Parija, A., *et al.* (2021). Electronic structure modulation of MoS_2 by substitutional Se incorporation and interfacial MoO_3 hybridization: Implications of Fermi engineering for electrocatalytic hydrogen and oxygen evolution. *Chemical Physics Reviews*, *2*(1). https://doi.org/10.1063/5.0037749

[30] Liu, P., *et al.* (2015). Interfacial electronic structure at the $CH_3NH_3PbI_3/MoO_x$ interface. *Applied Physics Letters*, *106*(19). https://doi.org/10.1063/1.4921339

[31] ASTM International. (2012). *Reference spectra derived from SMARTS v. 2.9.2 (ASTM G173-03)*. American Society for Testing and Materials.

[32] Adjouz, R., Allam, Z., Souli, L., Hafaifa, L., & Zebeir, A. (2024). Simulation and modeling of a new $CsSnI_3$ solar cell structure: A numerical study. *Semiconductor Science and Technology*, *39*(12), 125010. https://doi.org/10.1088/1361-6641/ad8ae2

[33] Sumona, F. B., Kashif, M., Danladi, E., Tighezza, A. M., Al-Mahmud, N., Toki, G. F. I., & Hossain, M. K. (2023). Optimization of perovskite $KSnI_3$ solar cell using different hole and electron transport layers: A numerical SCAPS-1D simulation. *Energy & Fuels*, *37*(23), 19207–19219. https://doi.org/10.1021/acs.energyfuels.3c02397

[34] Raeyani, D., & Asgari, A. (2023). Enhancing the efficiency of inverted organic solar cells with treatment techniques: Numerical and experimental study. *International Journal of Energy Research*, *2023*, 1–24. https://doi.org/10.1155/2023/6612574

[35] Chala, S., Boumaraf, R., Bouhdjar, A. F., Bdirina, M., Labed, M., Taouririt, T. E., Elbar, M., Sengouga, N., Yakuphanoğlu, F., Rahmane, S., Naoui, Y., & Benbouzid, Y. (2021). Synthesis and characterization of ZnO thin film for modeling the effect of its defects on ZnO/Cu_2O solar cell EQE. *Journal of Nano and Electronic Physics*, *13*(1), Article 01009. https://doi.org/10.21272/jnep.13(1).01009

[36] Hafaifa, L., Maache, M., & Bouabdelli, M. W. (2024). Improved performance of CdTe thin film solar cell through key parameters. *Journal of Theoretical and Applied Physics*, *18*(3), 1–10. https://doi.org/10.57647/j.jtap.2024.1803.35

[37] Das, S., Chakraborty, K., Choudhury, M. G., & Paul, S. (2021). Studies on thickness and internal quantum efficiency of $Cs_2AgBiBr_6$-based double perovskite material for photovoltaic application. *Journal of Nano and Electronic Physics*, *13*(3), Article 03018. https://doi.org/10.21272/jnep.13(3).03018

[38] Zaidi, B., Ullah, M. S., Zahra, S., Gagui, S., & Shekhar, C. (2021). Analysis of I–V–T characteristics of $CH_3NH_3PbBr_3$-based perovskite solar cells. *Journal of Nano and Electronic Physics*, *13*(5), Article 05016. https://doi.org/10.21272/jnep.13(5).05016

[39] Li, B., *et al.* (2020). Tin-based defects and passivation strategies in tin-related perovskite solar cells. *ACS Energy Letters*, *5*(12), 3752–3772.

[40] Cao, J., & Yan, F. (2021). Recent progress in tin-based perovskite solar cells. *Energy & Environmental Science*, *14*(3), 1286–1325.

[41] Mäckel, H., & MacKenzie, R. C. I. (2018). Determination of charge-carrier mobility in disordered thin-film solar cells as a function of current density. *Physical Review Applied*, *9*(3), 034020. https://doi.org/10.1103/PhysRevApplied.9.034020

[42] Greulich, J., Glatthaar, M., & Rein, S. (2012). Separation of series resistance and space charge region recombination in crystalline silicon solar cells from dark and illuminated current–voltage characteristics. *IEEE Journal of Photovoltaics*, *2*(2), 241–246. https://doi.org/10.1109/JPHOTOV.2012.2189370

[43] Chabri, I., Benhouria, Y., Oubelkacem, A., Kaiba, A., Essaoudi, I., & Ainane, A. (2023). Enhanced stability of γ-$CsSnI_3$-based perovskite solar cells by (γ-$CsSnI_3/Cs_2SnI_6$) heterojunction. *Solar Energy Materials & Solar Cells*. Advance online publication. https://doi.org/10.1016/j.solmat.2023.112426

[44] Xu, H., Guo, Z., Chen, P., & Wang, S. (2024). Toward durable all-inorganic perovskite solar cells: From lead-based to lead-free. *Chemical Communications*, *60*, 12287–12301. https://doi.org/10.1039/D4CC04000G

[45] Moone, P. K., & Sharifi, N. (2024). Performance and stability of all-inorganic and hybrid perovskites in planar FTO/SnO_2/perovskite/Cu_2O/carbon structures using SCAPS-1D simulation. *Journal of Optics*. Advance online publication. https://doi.org/10.1007/s12596-024-02168-3

[46] Das, S., Narzary, S., Chakraborty, K., & Paul, S. (2024). Effect of temperature on lead-free cesium-based double perovskite solar cells using SCAPS-1D. *Journal of Nano and Electronic Physics*, *16*(5), Article 05009. https://doi.org/10.21272/jnep.16(5).05009

[47] Aydin, E., De Bastiani, M., & De Wolf, S. (2019). Defect and contact passivation for perovskite solar cells. *Advanced Materials*, *31*(25), 1900428. https://doi.org/10.1002/adma.201900428

[48] Chen, J., & Park, N.-G. (2020). Materials and methods for interface engineering toward stable and efficient perovskite solar cells. *ACS Energy Letters*, *5*(8), 2742–2786. https://doi.org/10.1021/acsenergylett.0c01240

[49] Akin, S., Arora, N., Zakeeruddin, S. M., Grätzel, M., Friend, R. H., & Dar, M. I. (2020). New strategies for defect passivation in high-efficiency perovskite solar cells. *Advanced Energy Materials*, *10*(13), 1903090. https://doi.org/10.1002/aenm.201903090

[50] Jiao, S., Wang, T., & Zhou, Z. (2025). Additive engineering toward suppression of Sn^{2+} oxidation in Sn–Pb perovskite solar cells: Mechanisms, advances, and outlook. *ChemSusChem*. Advance online publication. https://doi.org/10.1002/cssc.202500333

[51] Alshaeer, F., *et al.* (2025). Synergistic defect passivation and charge transport enhancement via thiosemicarbazide-functionalized carbon nanotubes for high-efficiency lead-free $CsSnI_3$ perovskite solar

cells. *Journal of Alloys and Compounds, 1026*, 180428. https://doi.org/10.1016/j.jallcom.2025.180428

[52] Ye, T., Wang, K., Hou, Y., Yang, D., Smith, N., Magill, B., & Priya, S. (2021). Ambient-air-stable lead-free $CsSnI_3$ solar cells with greater than 7.5% efficiency. *Journal of the American Chemical Society, 143*(11), 4319–4328. https://doi.org/10.1021/jacs.0c13069

[53] Moone, P. K., & Sharifi, N. (2024). Comparison of Pb-based and Sn-based perovskite solar cells using SCAPS simulation: Optimal efficiency of eco-friendly $CsSnI_3$ devices. *Environmental Science and Pollution Research, 31*(39), 51447–51460. https://doi.org/10.1007/s11356-024-34622-x

[54] Bhattarai, S., *et al.* (2024). Enhancement of efficiency in $CsSnI_3$-based perovskite solar cells by numerical modeling of graphene oxide as HTL and ZnMgO as ETL. *Heliyon, 10*(1), e24107. https://doi.org/10.1016/j.heliyon.2024.e24107

[55] Alqahtani, R. T., Chrafih, Y., & Ajbar, A. (2025). Next-generation solar cells: Revealing the promise of $CsPbI_3/CsSnI_3$ tandem devices. *Solar Energy, 298*, 113665. https://doi.org/10.1016/j.solener.2025.113665

[56] Kaur, N., Madan, J., & Pandey, R. (2025). Numerical insights into MXene-integrated perovskite solar cells with compositionally engineered $CsSnI_{3-x}Br_x$ absorbers. *Materials Science and Engineering B, 318*, 118238. https://doi.org/10.1016/j.mseb.2025.118238